Optics and Lasers in Engineering 50 (2012) 703–709

Contents lists available at SciVerse ScienceDirect

Optics and Lasers in Engineering

journal homepage: www.elsevier.com/locate/optlaseng

Reconstruction of spatially misaligned and turbulence degraded images

Dongfeng Shi, Chengyu Fan*, Hong Shen, Haitao Wang, Huimin Ma, Chunhong Qiao, Xiaoxing Feng, Yingjian Wang

Key Laboratory of Atmospheric Composition and Optical Radiation, Anhui Institute of Optics and Fine Mechanics, Chinese Academy of Sciences, Hefei 230031, China

ARTICLE INFO

Article history:
Received 3 September 2011
Received in revised form
21 November 2011
Accepted 27 November 2011
Available online 20 December 2011

Keywords:
Atmospheric turbulence
Multiframe blind deconvolution
Image registration

ABSTRACT

A reconstruction method is presented to deal with spatially misaligned and turbulence degraded images that contain shift and rotation motion. This method is implemented through bringing the channels into spatial alignment via image registration and then restoring the original images by a new multiframe blind deconvolution. A frequency domain technique is introduced to precisely register the spatially misaligned images. New priori information of temporal signatures is adopted to constrain the solution in the blind deconvolution. Results show that by the proposed method high quality image can be recovered from spatially misaligned and turbulence degraded images.

1. Introduction

Atmospheric turbulence degrades the quality of images and video sequences. Turbulence causes spatially and temporally chaotic fluctuations in the refraction index of the atmosphere [1] and results in time-variant point spread function (PSF). The distorting effect of atmospheric turbulence becomes a severe problem, when one wishes for highly detailed images. Over the years many methods have been proposed to solve the problem. Deconvolution [2–5] seeks an estimate of the true image assuming that the PSF is exactly known. In practice, however, the PSF is estimated either theoretically or experimentally. Such estimates may deviate significantly from the true PSF, and thus the corresponding restored image may be unacceptable. Blind deconvolution is another important technique for restoring image when the PSF of the imaging system is unknown. Perhaps one of the most widely used blind restoration techniques is multiframe blind deconvolution (MFBD) [6–13]. This technique is used for multiframe images observed from stationary objects through different channels as a result of the time-variant PSF. And it has the main advantage of exploiting the diversity and redundancy information in different channels, and more importantly, it may lead to significant improvements in the restored image quality.

Stationary objects being observed through the atmosphere can waver spatially as if they are in motion. In many practical situations, the imaging is also influenced by some other factors: relative motion between camera and object, change of focus, or a combination of these two, and so forth. These will lead to spatial transformation (called channel misregistrations) that describes differences among the obtained images. For most MFBD methods, the channel misregistrations would lead to strong artifacts in the restored image [14]. Alternating minimization maximum a posterior (AM–MAP) [14] is the first method explicitly dealing with unregistration of images in multichannel framework. Unfortunately, only image shift is considered while rotation is ignored in this method.

In this paper, a reconstruction method is presented to deal with spatially misaligned and turbulence degraded images that contain shift and rotation motion. This method is implemented through bringing the channels into spatial alignment via image registration and then restoring the original images by a new multiframe blind deconvolution. For elastic image registration, there are several options: (i) correlation methods [15]; (ii) frequency domain methods [16,17]; (iii) graph-theoretic methods [18]. Here, a frequency domain technique [17] is introduced to precisely register the spatially misaligned and turbulence degraded images. Then a novel MFBD is employed to recover the original object image. As the blind deconvolution is an ill-posed problem, regularization is utilized. In addition, in order to find the unique and stable solution, priori information is employed to constrain the solution. New information of temporal signatures which is first exploited in [19] is applied, besides the basic prior information of non-negativity, finite support and normalization.

The rest of the article is organized as follows. Section 2 discusses the imaging model. The image registration algorithm is described in Section 3 and MFBD is presented in Section 4. In Section 5, we demonstrate the effectiveness of this method on

* Corresponding author.
E-mail address: cyfan@aiofm.ac.cn (C. Fan).

0143-8166/$ - see front matter Crown Copyright © 2011 Published by Elsevier Ltd. All rights reserved.
doi:10.1016/j.optlaseng.2011.11.018

spatially misaligned and atmospheric turbulence degraded images, and meanwhile conclusions and remarks are given in Section 6.

2. Imaging model

Within the isoplanatic angle, the detected intensity z_j at the focal plane of the imaging system is given by

$$z_j(\tau_j(x)) = (y \otimes h_j)(x) + n_j(x), \quad j = 1,\ldots,L, \tag{1}$$

where x is the spatial coordinate, L is the number of channels, h_j is the systemic PSF (blur), y is the original image and z_j is the observed degraded misaligned image. We assume that the noise field n_j in each channel is completely independent and has the standard Gaussian distribution. The symbol $\otimes$ denotes two-dimensional convolution. $\tau_j(x)$ describes geometric differences between the referenced channel and the jth channel. MFBD aims to recover the original image of stationary objects given a sequence of degraded misaligned images. Light emanating from the object is assumed to be incoherent. According to the Fourier optics [9], the PSF is completely characterized by the turbulence phase $\phi(x)$ in the pupil of the instrument:

$$h_j(x) = \left|FT^{-1}(p(x)e^{i\phi(x)})\right|^2, \tag{2}$$

where $p(x)$ is the pupil function (1 inside, 0 outside) and FT denotes the Fourier transformation.

3. Image registration

The shift and rotation motion can be estimated using the frequency domain approach. Assume we have an original image $z_1(x)$, and its rotated and shifted image $z_2(x)$:

$$z_2(x) = z_1(Rx + \Delta x),$$

with

$$x = \begin{bmatrix} x_1 \\ x_2 \end{bmatrix}, \quad \Delta x = \begin{bmatrix} \Delta x_1 \\ \Delta x_2 \end{bmatrix}, \quad R = \begin{bmatrix} \cos\phi & \sin\phi \\ -\sin\phi & \cos\phi \end{bmatrix}.$$

According to the Fourier translation and rotation property, transforms of $z_1(x)$ and $z_2(x)$ are related by

$$Z_2(u,v) = e^{j2\pi(u\Delta x_1 + v\Delta x_2)} Z_1(u\cos\phi + v\sin\phi, -u\sin\phi + v\cos\phi),$$

where (u,v) are the coordinates in the frequency space. Let M_1 and M_2 be the amplitudes of Z_1 and Z_2, respectively. The following result is derived:

$$M_2(u,v) = M_1(u\cos\phi + v\sin\phi, -u\sin\phi + v\cos\phi).$$

It is clear that when the image is rotated over the angle ϕ in the spatial domain, the value of frequency has the same rotation (see Fig. 1 which shows the original image, the rotated image and their frequency values). In the light of this point, a method is introduced to calculate the rotation angle. First, the spectrum is translated to polar coordinates, and then we define the frequency content q as a function of the angle α by integrating over radial lines:

$$q(\alpha) = \sum_{\theta=\alpha-\Delta\alpha}^{\alpha+\Delta\alpha} \sum_{r=0}^{\infty} M(r,\theta). \tag{3}$$

The low frequencies generally contain most of the energy and introduce large calculation error. Most of the high frequencies are always composed of the noise signal for a noisy degraded image. Thus $q(\alpha)$ is only evaluated on a circular disk limited by $\rho_1 < r < \rho_2$. The function q for both M_1 and M_2 (Fig. 1(e)) is obtained. Then the exact rotation angle can be computed when the q values of M_1 and M_2 reach the maximum.

When the rotation is eliminated, the images only contain the shift motion differences. A shift of the image paralleling to the original image plane can be expressed as a linear phase shift in the frequency domain:

$$Z_2(u,v) = e^{j2\pi(u\Delta x_1 + v\Delta x_2)} Z_1(u,v). \tag{4}$$

The shift parameters can be computed as the slope of phase difference. In order to eliminate the influence of the noise, we only use the low frequencies to calculate the shift motion.

4. Multiframe blind deconvolution

We employ the MFBD to obtain the original object image using the registered images $z_j^{\oplus}(x)$. For the MFBD, the cost function [20] is introduced

$$J(y,h) = \sum_{j=1}^{L} \left\| z_j^{\oplus} - (y \otimes h_j)^2 \right\| + \lambda_1 r(y) + \lambda_2 \sum_{j=1}^{L} r(h_j).$$

When $r(y) = \|y\|^2$ and $r(h_j) = \|h_j\|^2$, according to the Parseval theorem the above formulation can be expressed in the frequency domain as

$$J(Y,H) = \sum_{j=1}^{L} \|Z_j - YH_j\|^2 + \lambda_1 \|Y\|^2 + \lambda_2 \sum_{j=1}^{L} \|H_j\|^2. \tag{5}$$

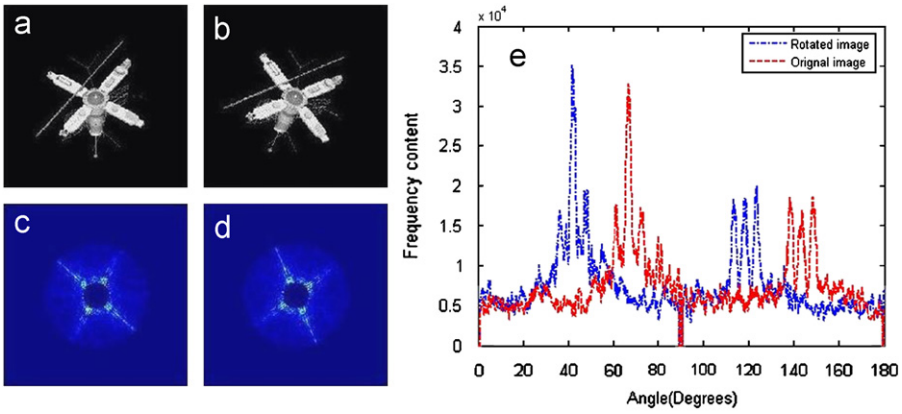

Fig. 1. (a) Original image, (b) Rotated image, (c) and (d) Amplitudes of frequency values of the original image and the rotated image for $0.1\rho < r < 0.4\rho$, respectively, and (e) Function q for both (c) and (d).

where λ_1, λ_2 are the regularization parameters, and Y, H_j, Z_j are the Fourier transforms of y, h_j, $z_j^{\oplus}$, respectively. This approach of treating the data frames to be independent of each other and allocating variables to describe each of the $L+1$ "convolution components" of the data set is typical for MFBD algorithms. In [19], the authors refer to it as "traditional" MFBD.

The observed images are of short exposure duration, of the order of 1/60 s or less, but are separated in time by more than one short exposure duration, say, 3/60 s. Then, the observed images see independent turbulence phase distributions across the optical pupil. In the absence of noise, the spectral ratio (Z_i/Z_j) for any two registered images i, j is independent of the unknown object and provides a measure of the change in the ratio of (H_i/H_j). Thus, if H_j is known, by using the observed spectral ratios, the remaining H_i can be determined $(H_i=H_j[Z_i/Z_j])$. In [20–22], they use this relationship to get the PSF and then inverse it to restore the original image. This method is referenced as "image division". In this paper, we model the cost function by the spectral ratio. When we estimate the H_j, a number of additional control frames, which are the ith frames ($i=1,\ldots,L$ and $i\neq j$), are employed to constrain the solution. Control term which is beneficial to get the optimal restored image is added in the cost function Eq. (5)

$$J(Y,H)=\sum_{j=1}^{L}\|Z_j-YH_j\|^2+\lambda_1\|Y\|^2+\lambda_2\sum_{j=1}^{L}\|H_j\|^2+\lambda_3 \times\sum_{j=1}^{L}\sum_{i=1,i\neq j}^{L}\|Z_iH_j-Z_jH_i\|^2, \tag{6}$$

where λ_3 is the regularization parameter.

An alternating minimization method is applied to recover the image and simultaneously identify the point spread function. With the initial guesses of image $Y^{(0)}$ and PSFs $H^{(0)}$, the values $Y^{(n)}$ and $H^{(n)}$ can be procured through approaching the cycle between the image subspace and PSFs subspace estimation steps. The two iterative steps are:

$$Y^{(n+1)}=Y^{(n)}-\alpha\partial_{Y^*}J(Y^{(n)},H^{(n)})/\partial_Y\partial_{Y^*}J.$$

$$\Leftrightarrow Y^{(n+1)}=(1-\alpha)Y^{(n)}+\alpha\sum_{j=1}^{L}Z_jH_j^{*(n)}/\left(\sum_{j=1}^{M}|H_j^{(n)}|^2+\lambda_1\right).$$

$$H_j^{(n+1)}=H_j^{(n)}-\beta\partial_{H_j^*}J(Y^{(n+1)},H_j^{(n)})/\partial_{H_j}\partial_{H_j^*}J.$$

$$\Leftrightarrow H_j^{(n+1)}=(1-\beta)H_j^{(n)}+\beta\left(Z_jY^{*(n+1)}+\lambda_3Z_j\sum_{i=1,i\neq j}^{L}Z_i^*H_i^{(n)}\right)\Big/\left(|Y^{(n+1)}|^2+\lambda_3\sum_{i=1,i\neq j}^{L}|Z_i|^2+\lambda_2\right).$$

Here, the parameters α, β are the step sizes in the recursions. In our experiments, we set $Y^{(0)}$ to be the average frequency value of the registered images and $H^{(0)}$ to be a delta function. The minimization may not have a unique solution because of the noise in the image. In order to get the meaningful solution, the noise needs to be restrained. In this paper, the adaptive normalized convolution [23] is utilized to filter the image at each iterative step for restraining noise. The method employs an anisotropic Gaussian kernel that adapts its shape and orientation along the underlying image structure to allow better noise suppression while avoid image blurring across lines and edges. And the shape and orientation of the kernel in the noisy case are very close to those of the noise-free case. Because of the stabilization of the kernel, the adaptive normalized convolution is employed in our method.

The adaptive normalized convolution is defined as:

$$z(\mathbf{x})=\sum_t K_T(\mathbf{x}_t-\mathbf{x})y_t^{(n)}/\sum_t K_T(\mathbf{x}_t-\mathbf{x}),$$

where $K_T(x_t-x)$ is the data-adaptive kernel function, $z(x)$ is the true pixel value which we wish to reconstruct at the position x, and $y_t^{(n)}$ is the tth sample of the recovered image in the spatial domain at the position x_t within a local neighborhood of which the center is x.

The $K_T(x_t-x)$ can be written as

$$K_T(\mathbf{x}_t-\mathbf{x})=c(\mathbf{x},\mathbf{x}_t)a(\mathbf{x},\mathbf{x}_t),$$

where $c(x,x_t)$ and $a(x,x_t)$ are the robust certainty and structure-adaptive applicability function, respectively, which can be expressed as

$$c(\mathbf{x},\mathbf{x}_t)=\exp(-|y_t^{(n)}(\mathbf{x}_t)-y^{(n)}(\mathbf{x})|^2/2\zeta^2),$$

$$a(\mathbf{x},\mathbf{x}_t)=\rho(\mathbf{x}-\mathbf{x}_t)\exp[-((x_1\cos\phi+x_2\sin\phi)/\sigma_u(\mathbf{x}))^2-((-x_1\sin\phi+x_2\cos\phi)/\sigma_v(\mathbf{x}))^2],$$

where parameter ζ defines an acceptable range of the residual error $|y_t^{(n)}(\mathbf{x}_t)-y^{(n)}(\mathbf{x})|$ and $\rho(x-x_t)$ limits the support of the kernel within an area of a certain radius. The parameters $\sigma_u(x)$ and $\sigma_v(x)$ are the directional scales of the structure-adaptive applicability function. The details of estimating these parameters using the method in [24] are described as follow:

$$G=\begin{bmatrix}\vdots & \vdots\\ I_{t,x_1}^{(n)} & I_{t,x_2}^{(n)}\\ \vdots & \vdots\end{bmatrix}=U_tS_tV_t^{Tr},$$

where $I_{t,x_1}^{(n)}$ and $I_{t,x_2}^{(n)}$ are the first derivatives along x_1 and x_2 directions for the local image $y_t^{(n)}$, respectively. The second column of the 2×2 orthogonal matrix V_t, $v_2=[v_1,v_2]^{Tr}$, defines the dominant orientation angle ϕ

$$\phi=\arctan\left(\frac{v_1}{v_2}\right).$$

The diagonal 2×2 matrix S_t represents the energy in the dominant directions. The directional scales $\sigma_u(x)$ and $\sigma_v(x)$ can be defined by

$$\sigma_v(\mathbf{x})=\frac{s_1+\lambda'}{s_2+\lambda'},\quad \sigma_u(\mathbf{x})=1/\sigma_v(\mathbf{x}),$$

where λ' is the regularization parameter equal to $\lambda'=1.0$.

5. Numerical experiments

In this section, the method in this paper is tested by applying it to restore the noisy short exposure turbulence degraded misaligned images. We also perform comparisons with multichannel alternating minimization (MC–AM) published in [7] for recovering the original image. The measure that we used for evaluating the quality of the restored images is the root mean square error (RMSE). It can be computed as

$$\mathrm{RMSE}=\sqrt{\frac{1}{N_1N_2}\sum_{n_1,n_2}(y_t(n_1,n_2)-y_r(n_1,n_2))^2},$$

where N_1 and N_2 are the number of the pixels in the image along x_1 and x_2 directions, respectively, and (n_1,n_2) denotes location in the image, y_t is the original image, and y_r is the restored image.

All experiments are performed using three degraded misaligned images ($L=3$) and the same values for parameters: $\lambda_1=\lambda_2=10^{-5}$, $\lambda_3=1.2$, $\alpha=0.9$, and $\beta=0.6$. Fig. 1(a) is the original image. We generate turbulence phases that follow the Kolmogorov turbulence model [1] using Fourier transform method. The simulated speckle

PSF is computed by Eq. (2). We simulate the turbulence degraded images recorded by a 0.8 m telescope with the atmospheric seeing parameter $r_0=13$ cm($D/r_0\sim6.15$, where D is the diameter of the telescope aperture). Different amounts of white Gaussian noise, which can be expressed as blurred signal-to-noise ratio (BSNR), are added to test the algorithm's robustness against noise. The BSNR is

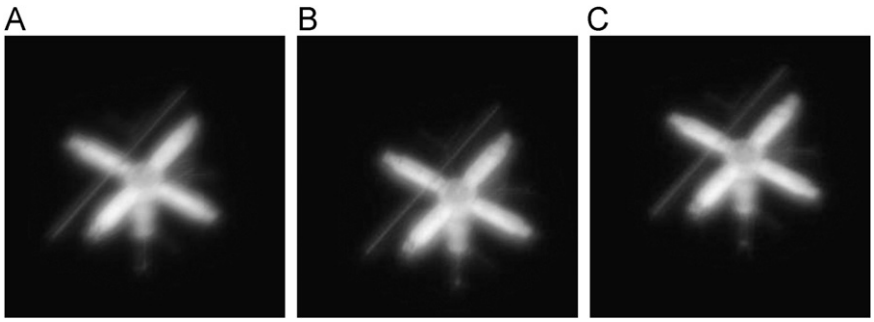

Fig. 2. Blurred noise-free misaligned images: (A) First channel (B) Second channel (shifted by [1620] pixels), and (C) Third channel (shifted by [−20 15] pixels).

Table 1
Estimated results of Shift(S) and Rotation(R).

BSNR		#1	#2	#3	
		S (Pixel)	R (Degree)	S (Pixel)	R (Degree)
0 dB	F. 2	15.68 20.10	29.8	17.70 −19.92	−15.1
	F. 3	−19.60 15.66	−24.9	−14.60 16.66	26.0
40 dB	F. 2	15.68 20.10	29.8	17.70 −19.92	−15.1
	F. 3	−19.60 15.66	−24.4	−14.60 16.66	26.0
30 dB	F. 2	15.68 20.08	29.8	17.70 −19.94	−15.1
	F. 3	−19.59 15.65	−24.4	−14.64 16.68	26.2

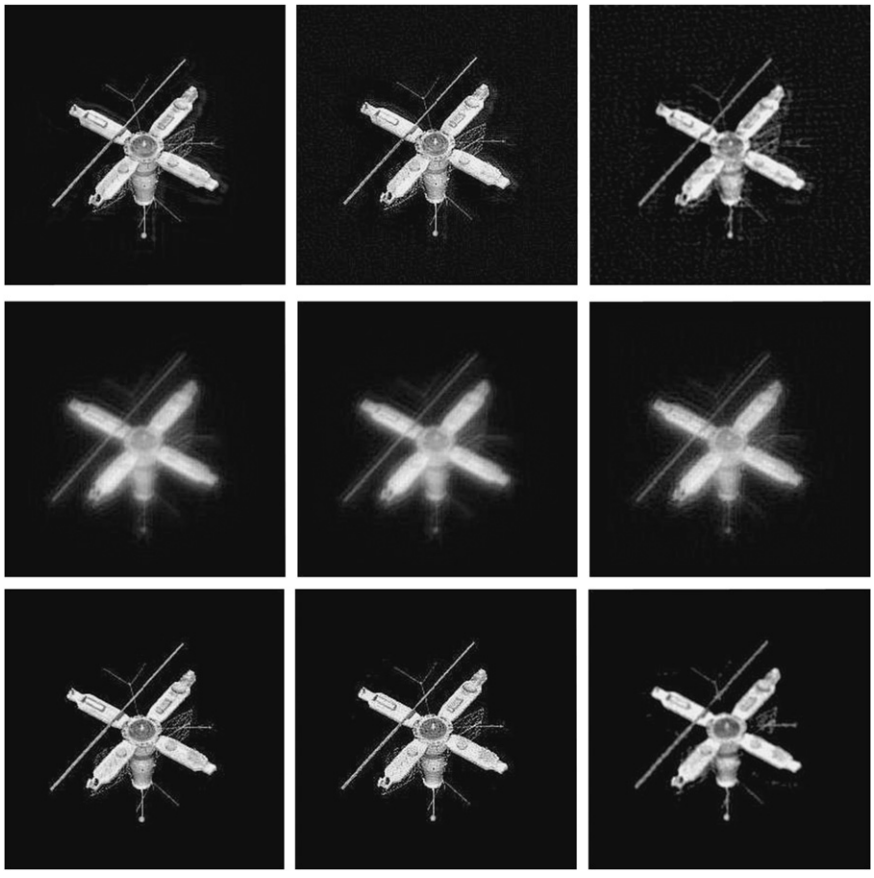

Fig. 3. Deblurred images: First row: images deblurred with our MFBD using the misaligned images (MFBD–MI); Second row: images deblurred with MC–AM using the registered images (MC–AM–RI); Third row: images deblurred with our MFBD using the registered images (MFBD–RI).

Table 2
Summary of the RMSE values obtained with MFBD–MI, MC–AM–RI, and MFBD–RI.

BSNR		MFBD–MI	MC–AM-RI	MFBD–RI
0 dB	#1	8.91	24.90	6.52
	#2	25.98	24.81	13.92
	#3	27.87	25.88	8.91
40 dB	#1	10.67	24.864	9.34
	#2	41.12	25.05	14.08
	#3	44.46	24.09	13.50
30 dB	#1	14.38	24.94	12.35
	#2	45.98	24.64	14.66
	#3	50.54	26.41	13.74

given by:

$$\mathrm{BSNR} = 10\log_{10}\frac{1}{\sigma^2 N_1 N_2}\sum_{n_1,n_2}\left((y\otimes h)(n_1,n_2) - \frac{1}{N_1 N_2}\sum_{n_1,n_2}(y\otimes h)(n_1,n_2)\right)^2.$$

The noisy degraded images are translated by applying some known transformations. We give three sets of planar motion situations: #1 the second and third noisy degraded images are shifted by [1620] and [−20 15] pixels respectively and not rotated; #2 the second and third noisy degraded images are rotated by 30 and −25 degrees respectively and not shifted; #3 the second and third noisy degraded images are shifted by [18–20] and [−15 16] pixels, and rotated by −15 and 26 degrees, respectively. The first image is chosen as the referenced image.

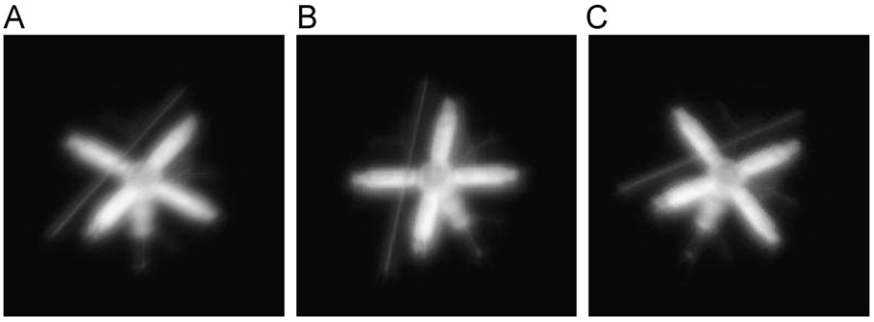

Fig. 4. Blurred noise-free misaligned images: (A) First channel (B) Second channel (rotated by 30 degrees), and (C) Third channel (rotated by −25 degrees).

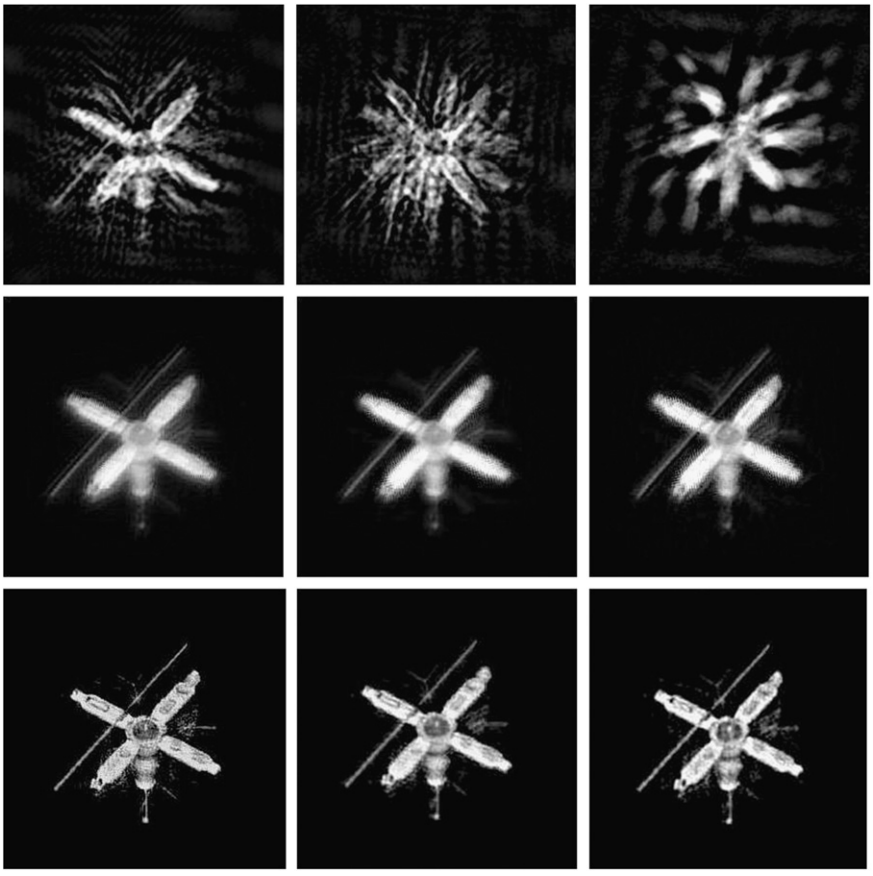

Fig. 5. Deblurred images: First row: images deblurred with MFBD–MI; Second row: images deblurred with MC–AM–RI; Third row: images deblurred with MFBD–RI.

The blurred noise-free misaligned images in situation #1 are shown in Fig. 2. Estimated results of Shift(S) are shown in Table 1. We can see that the registration method with subpixel accuracy has stabilization even the images stained by different amount of noise. The deblurred images that are obtained by the method in [7] and our method are shown in Fig. 3 with BSNRs of 0 dB, 40 dB and 30 dB, respectively. The results show that the quality of the deblurred images is slightly influenced when the images only contain the shift motion for our method and high quality images can be restored by our method using the registered images. Table 2 gives the RMSE values. The results prove the validity of our method.

Fig. 4 shows the blurred misaligned images in situation #2. Estimated results of Rotation(R) are shown in Table 1. The results show that the registration method with subdegree accuracy possesses the capability of having meaningful estimates even at different levels of BSNR. The images recovered by the two methods are shown in Fig. 5 with BSNRs of 0 dB, 40 dB and 30 dB, respectively. The results demonstrate two important points. First, MFBD using the images that contain rotation motion leads to unacceptable results and the registration method for correcting the rotation must be employed. Second, our MFBD method using the registered images provides high fidelity solutions. The RMSE values of the results are shown in Table 2 and accordant with the previous points.

The blurred misaligned images are shown in Fig. 6 in situation #3. Table 1 shows estimated results of Shift(S) and Rotation(R). We can get the similar conclusion that the registration method with subpixel and subdegree accuracy has stabilization even the images stained by different amount of noise. The reconstruction images obtained by the two methods are shown in Fig. 7 with BSNRs of 0 dB, 40 dB and 30 dB, respectively. It shows that more unacceptable results will be achieved when the images contain both shift and rotation and our MFBD method using the registered

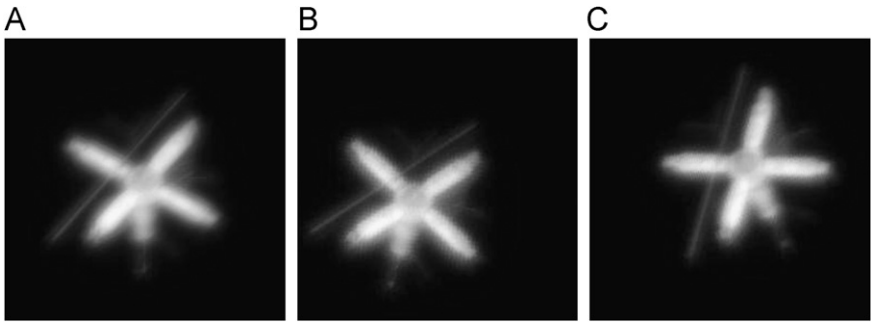

Fig. 6. Blurred noise-free misaligned images: (A) First channel (B) Second channel (shifted by [18–20] pixels and rotated by -15 degrees), and (C) Third channel (shifted by [-15 16] pixels and rotated by 26 degrees).

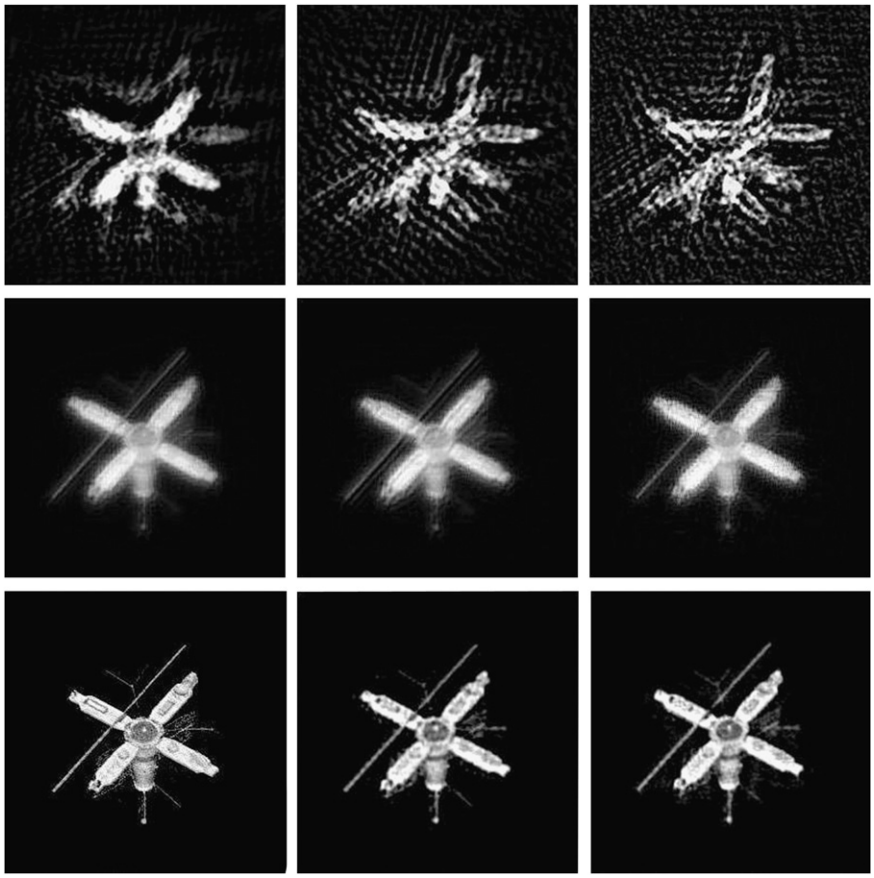

Fig. 7. Reconstruction of images: First row: images deblurred with MFBD–MI; Second row: images deblurred with MC–AM–RI; Third row: images deblurred with MFBD–RI.

images leads to high accuracy results. Table 2 shows a summary of the RMSE values accordant with the previous conclusion.

6. Conclusion

A reconstruction method for spatially misaligned and turbulence degraded images is presented. This method uses a combination of techniques: image registration technique which brings the channels into spatial alignment, and a new MFBD technique which applies new priori information of temporal signatures. The shift and rotation can be estimated with subpixel and subdegree error utilizing the effective image registration technique. Then a high resolution image is reconstructed from the registered images through the MFBD method. The results show that the quality of the recovered images is slightly influenced when the images only contain the shift motion, but if the rotation exists, the recovered image is unacceptable and image registration must be employed to remove the geometric differences. At least two interesting aspects need further development and exploration, that is, more accurate method to estimate the rotation and the relationship between the estimated error of the rotation and the quality of the recovered image.

This work is supported by Hefei Institutes of Physical Sciences, Chinese Academy of Sciences (Grant Nos. 073RC11123, Y03RC21121 and XJJ-11-S106).

References

[1] Roggemann MC. Imaging through turbulence. Boca Raton: CRC Press; 1995.
[2] Yitzhaky Y, Dror I, Kopeika NS. Restoration of atmospherically blurred images using weather-predicted atmospheric modulation transfer function (MTF) [J]. Image Propag. Atmos. 1996;2828:386–96.
[3] Primot J, Rousset G, Fontanella JC. Deconvolution from wave-front sensing: a new technique for compensating turbulence-degraded images [J]. J. Opt. Soc. Am. A 1990;7:1598–608.
[4] Roggemann MC, Welsh BM. Signal-to-noise ratio for astronomical imaging by deconvolution from wave-front sensing [J]. Appl. Opt. 1994;33:5400–14.
[5] Welsh BM, Roggemann MC. Signal-to-noise comparison of deconvolution from wave-front sensing with traditional linear and speckle image reconstruction [J]. Appl. Opt. 1995;34:2111–9.
[6] Zhulina YV. Multiframe blind deconvolution of heavily blurred astronomical images [J]. Appl. Opt. 2006;45:7342–52.
[7] Sroubek F, Flusser J. Multichannel blind iterative image restoration [J]. IEEE Trans. Image Process. 2003;12:1094–106.
[8] Vorontsov SV, Strakhov VN, Jefferies SM, Borelli KJ. Deconvolution of astronomical images using SOR with adaptive relaxation. Opt. Express 2011;19:13509–24.
[9] Jefferies SM, Hart M. Deconvolution from wave front sensing using the frozen flow hypothesis,. Opt. Express 2011;19:1975–84.
[10] Hirsch M, Harmeling S, Sra S, Schölkopf B. Online multi-frame blind deconvolution with super-resolution and saturation correction. A & A 2011;531:A9.
[11] Wen Y-W, Liu C, Yip AM. Fast splitting algorithm for multiframe total variation blind video deconvolution. Appl. Opt. 2010;49:2761–8.
[12] Souidene W, Abed-Meraim K, Beghdadi A, New A. Look to Multichannel Blind Image Deconvolution. IEEE Trans. Image Process. 2009;18:1487–500.
[13] G. Cristobal, F. Sroubek, J. Flusser, Multiframe Blind Deconvolution Coupled with Frame Registration and Resolution Enhancement. In: Blind Image Deconvolution, CRC Press, 2009.
[14] Sroubek F, Flusser J. Multichannel blind deconvolution of spatially misaligned images [J]. IEEE Trans. Image Process. 2005;14:874–83.
[15] Barnea DI. and Silverma.Hf, CLASS OF ALGORITHMS FOR FAST DIGITAL IMAGE REGISTRATION. IEEE Trans. Comput. C 1972;21. 179.
[16] Reddy BS, Chatterji BN. An FFT-based technique for translation, rotation, and scale-invariant image registration. IEEE Trans. Image Process. 1996;5: 1266–71.
[17] Vandewalle P, Susstrunk S, Vetterli M. A frequency domain approach to registration of aliased images with application to super-resolution. Eurasip J. Appl. Signal Process. 2006;2006 14 pp.
[18] Brown LG. A SURVEY OF IMAGE REGISTRATION TECHNIQUES. Comput. Surv. 1992;24:325–76.
[19] Hope DA, Jefferies SM. Compact multiframe blind deconvolution. Opt. Lett. 2011;36:867–9.
[20] Souidene W, Abed-Meraim K, Beghdadi A. A New Look to Multichannel Blind Image Deconvolution. IEEE Trans. Image Process. 2009;18:1487–500.
[21] Barraza-Felix S, Frieden BR. Regularization of the Image Division Approach to Blind Deconvolution. Appl. Opt. 1999;38:2232–9.
[22] Frieden BR. An exact, linear solution to the problem of imaging through turbulence. Opt. Commun. 1998;150:15–21.
[23] Pham TQ, van Vliet LJ, Schutte K. Robust fusion of irregularly sampled data using adaptive normalized convolution [J]. Eurasip J. Appl. Signal Process. 2006.
[24] Takeda H, Farsiu S, Milanfar P. Kernel regression for image processing and reconstruction [J]. IEEE Trans. Image Process. 2007;16:349–66.